OPTIMAL GUIDANCE AND DECENTRALISED STATE ESTIMATION APPLIED TO A FORMATION FLYING DEMONSTRATION MISSION IN GTO[1]

Dan Dumitriu[*,2], Sónia Marques[*], Pedro U. Lima[*], Juan C. Bastante[†], João Araújo[‡], Luis F. Peñín[‡], Augusto Caramagno[‡], Bogdan Udrea[§]

[*] *Instituto de Sistemas e Robótica, Instituto Superior Técnico, Av. Rovisco Pais 1, 1049-001 Lisbon, Portugal. Emails: {ddumitriu,sm3,pal}@isr.ist.utl.pt*

[†] *DEIMOS Space S.L. - Ronda de Poniente, 19; Edificio Fiteni VI, Portal 2, 2ª Planta; 28760 Tres Cantos; Madrid, Spain. Email: juan-carlos.bastante@deimos-space.com*

[‡] *DEIMOS Engenharia S.A -, Av. D. João II, Lt. 1.17, Edificio Torre Zen, 8ºB, 1998-022, Lisbon, Portugal. Emails: {augusto.caramagno,joao.araujo}@deimos.com.pt; luis-felipe.penin@deimos-space.com*

[§] *ESA/ESTEC - Keplerlaan 1, Postbus 299, 2200 AG Noordwijk, Netherlands. Email: Bogdan.Udrea@esa.int*

Abstract: This paper introduces an integrated approach to Guidance, Navigation and Control (GNC) of formation flying spacecraft. The design process considers a 3-spacecraft mission in a reference Geostationary Transfer Orbit (GTO). A detailed definition of the mission framework, in terms of GNC modes and corresponding science and technology requirements, is provided. This, together with an analysis of the dynamic environment of the mission, establishes the inputs to the design of a low-thrust optimal relative configuration that minimises the fuel consumption and overall complexity. The obtained solution is assessed in detail by means of an analysis considering perturbations acting over a spacecraft in Earth GTO. The GNC closed loop uses the results of the mission analysis and design process as specifications. An algebraic closed-loop algorithm is proposed for the Guidance and Control (GC) subsystem, minimizing the propellant consumption and ensuring collision avoidance. Using Pontryagin's Maximum Principle, the GC algorithm provides the optimal trajectories from the current state until the target state, as well as the optimal control inputs to follow these trajectories. A full-order decentralized filter implements the Navigation algorithm. It estimates the full state of the involved spacecraft and is based on an Extended Kalman Filter (EKF) for local measurements, and on a Covariance Intersection algorithm (plus the EKF prediction part) for the fusion between local state estimates and state estimates communicated by other spacecraft. Results of applying the GNC algorithms to a realistic simulation of the specified mission are presented. The main original contribution of the work presented here is the design of the formation flying mission and algorithms using a top-down approach. From a requirement to maximize the time which can be used for experimentation at the apogee the orbits of the three spacecraft, as well as the propellant optimal manoeuvres for formation (re)acquisition have been determined. A novel approach to the covariance intersection method has been used to estimate the relative positions between the spacecraft. The algorithms have been implemented and tested in an end-to-end mission simulation tool.

[1] This work has been developed under the ESA project "Formation Estimation Methodologies for Distributed Spacecraft" (FEMDS), ESA contract nº 17529/03/NL/LvH/bj.

[2] Dan Dumitriu is currently a researcher at the Institute of Solid Mechanics, Romanian Academy, Str. Constantin Mille, nr. 15, Bucharest, Romania.

Glossary of acronyms and symbols:

FEMDS	=	Formation Estimation Methodologies for Distributed Spacecraft
FF-FES	=	Formation Flying Function Engineering Simulator
GNC	=	Guidance, Navigation and Control
GC	=	Guidance and Control
GTO	=	Geostationary Transfer Orbit
LVLH	=	Local Vertical Local Horizon frame
IPQ	=	Inertial Planet Frame
FAC	=	Formation Acquisition mode
LFM	=	Loose Formation Mode
IFM	=	Interferometer Construction Mode
BCM	=	Baseline Control Mode
PMP	=	Pontryagin's Maximum Principle
EKF	=	Extended Kalman Filter
CI	=	Covariance Intersection algorithm
TF	=	Telescope Flyer
RF	=	Radio Frequency
s/c	=	spacecraft

$\boldsymbol{\rho}_{ij} = \left[x_{ij}\ y_{ij}\ z_{ij}\right]^T$	=	relative position vector between spacecraft *i* and spacecraft *j*
$\boldsymbol{\rho}'_{ij}$	=	relative velocity vector (derivative of $\boldsymbol{\rho}_{ij}$ with respect to the true anomaly ν)
ν	=	true anomaly at time *t*
a	=	orbit's semi-major axis
e	=	eccentricity of the orbit
Ω	=	right ascension of the ascending node (RAAN)
i	=	inclination of the orbit
ω	=	argument of perigee
M	=	mean anomaly
t_p	=	the passage time at perigee
n	=	natural frequency of the reference orbit
$\mathbf{k}_x$, $\mathbf{k}_y$, $\mathbf{k}_z$	=	axes of the Local Vertical Local Horizon frame
$\mathbf{x}_{IPQ}$, $\mathbf{y}_{IPQ}$, $\mathbf{z}_{IPQ}$	=	axes of the Inertial Planet Frame
D	=	distance between satellites
α	=	angle at the reference spacecraft
$\mathbf{X}$	=	state vector of the spacecraft formation
$\boldsymbol{\Lambda}$	=	co-state vector introduced by the PMP formulation
$\mathbf{U}$	=	control inputs vector for the spacecraft formation
$u_{\min}$, $u_{\max}$	=	control inputs limitations (minimum and maximum values)
J	=	cost function to be minimized in order to reduce the propellant consumption
$\hat{\mathbf{X}}^i$	=	state estimate vector at s/c *i*
$\mathbf{Q}$	=	covariance matrix of the process noise
$\boldsymbol{\Phi}_k$	=	transition matrix
T_s	=	sampling period used to propagate the estimate
$\mathbf{H}^i$	=	observation matrix at s/c *i*
$\mathbf{S}^i$	=	innovation covariance matrix at s/c *i*
$\mathbf{K}^i$	=	Kalman Gain at s/c *i*
$\mathbf{P}^i$	=	error covariance matrix at s/c *i*
ρ_i^j	=	code phase between transmitting spacecraft *i* and receiver spacecraft *j*
$\varepsilon_\rho^{i,j}$	=	pseudo-range measurement noise due to the receiver thermal noise
$E_{multipath}^{i,j}$	=	multi-path error

1 INTRODUCTION

A current and/or future trend in space science missions is the usage of several spacecraft flying in formation, in order to achieve higher accuracy in Earth and extra solar planetary observations, or higher region coverage when monitoring science data, than what would be possible by using monolithic platforms. Examples of this interest are the ESA DARWIN, LISA and NASA Earth Observing-1, Origins' NGST and TPF planned missions.

The goal of the ESA "Formation Estimation Methodologies for Distributed Spacecraft" (FEMDS) project was to extend the traditional Guidance, Navigation and Control (GNC) loop for a single spacecraft (s/c) to a set of s/c flying in formation. This paper summarizes the main results of the project. The mission design process, considers a 3-spacecraft formation flying demonstration mission in Geostationary Transfer Orbit (GTO). This study provided the formation design, the required modes for the mission, as well as initial and final formation state conditions for each mode. Those conditions were then used in the functional design and Matlab/Simulink implementation of the developed GNC algorithms. The algorithms were implemented and tested in DEIMOS' orbital dynamics simulator, known as the Formation Flying Function Engineering Simulator (FF-FES). The GNC tests described here were mainly concerned with the formation acquisition mode (FAC), the initial mode of the mission, where the 3 s/c are brought from a random disposition in a sphere of 8km diameter to a circle of 250m radius.

In order to have a mission frame defined with the required detail level, one of the first accomplished tasks was the design of a mission timeline with the definition of formation topology and the corresponding GNC modes. The definition of the formation topology consisted of searching for stable formation configurations around the apogee of the GTO reference orbit. Considering the typical set of pointing requirements for Darwin-like missions, stability is understood as: minimum variance of distances between s/c; minimum variance of angles between s/c; and minimum variance of spacecraft plane orientation. These configurations allow for a certain time interval for experimentation around apogee where minimum control action is required. An analytical design methodology has been used, based on a formulation relating the relative evolution of the Cartesian coordinates on a local frame

with the corresponding variations in the Keplerian elements between s/c. After obtaining a nominal design based on Keplerian dynamics, a numerical optimisation method is used to derive optimal low thrust profiles to fulfil imposed requirements on formation geometry.

Published work on formation flying GNC (for a practical engineering approach to s/c dynamics and control, see [16]; relative motion equations, relevant for formation flying s/c, and their solution are covered in [1],[15]) does not usually include a mission analysis part (with a few exceptions, e.g., [3], but for simplified scenarios), and typically concentrates on guidance and control ([4], [5], [8], [9], [10]) or navigation ([11], [12], [14]).

In [8] a methodology for deep space missions based on algebraic methods is used to allow the selection of the minimum amount of communication links between the spacecraft. This work considers a rigid formation of a set of spacecraft where linear dynamics is assumed. Each spacecraft is assumed to sense its position relative to the other spacecraft. An approach for the control of a spacecraft formation is reported in [5], where Linear Programming is used together with constraints to achieve a desired mission, using dynamics for the relative position of the spacecraft and again assuming perfect range sensing. The goal is to optimize the trajectories of the formation given an initial location and taking a reasonably small amount of time. Fuel optimized formation-keeping control is required to maintain the vehicles within a specified tolerance of the desired locations for each spacecraft in the fleet. In [9] a linear vehicle dynamics is used together with the minimization of a cost functional, which ensures stability, performance and obstacle/collision avoidance. Separate costs are assigned to the formation stabilization, obstacle avoidance and tracking of a desired trajectory. The technique is based on a two-dimensional triangular graph and on the definition of subgroups of core and follower vehicles. The optimal path for each vehicle is obtained in a centralized way, but the distribution of the computational load over the vehicles is also discussed. Singh and Hadaegh [10] introduced an optimal formulation of the guidance problem for spacecraft formations, which allows formation reconfiguration and is based on splines. The optimal spline parameters are determined by their method.

In reduced-order decentralized filters, to reduce the communication among the entire fleet, only local observations are used for the updating procedure, in a local filter, of the local state part of the

entire formation state. The local state is then sent to another s/c. The procedure repeats cyclically in a loop around all s/c, until the changes to the entire fleet state are small. By doing so, a fully connected communications network is avoided and also the computational load related to the computation of the entire fleet state estimates. This way, the measurements obtained from the formation flying spacecraft are used in a decentralized manner since the local filter in each spacecraft uses only local measurements reducing the computational load for computing the measurement update procedure. However, for most GC algorithms, a full state estimate is needed at each spacecraft. Thus, it is convenient to devise algorithms that estimate the full state without a fully connected communications network, and without a central estimator spacecraft that joins all the local information, as in [14]. Another problem is that the local measurements are function of other spacecraft state. Thus, the local observation equation update depends on the estimation of other spacecraft states. The solution for this problem consists of decoupling the local measurements which are function of more than one vehicle state. However the updating process takes 3-4 iterations [12] around the entire fleet, before the fleet state converges.

Given the mission requirements, GNC algorithms were designed, implemented and tested with the goal of enforcing the mission specifications along the orbit, in the presence of several differences with respect to the nominal design, e.g., perturbations acting over a spacecraft in Earth GTO, mismatches between actual and modelled relative dynamics, and sensor noise. For Guidance and Control (GC) of formation flying spacecraft, an optimal trajectory planning algorithm that minimizes the propellant consumption is used [6]. This closed-loop GC algorithm computes the s/c trajectories from the knowledge of the formation linearised dynamics and full state, and is similar to Tillerson's algorithm [5], although the optimal solutions are obtained using Pontryagin's Maximum Principle (PMP) [7], providing some advantages with respect to Tillerson's linear programming method, such as a simpler way of finding the solutions of the problem, and improved ability to consider non-linear perturbation models. To take the unmodeled perturbations into account, as well as the state estimation errors, the closed-loop GC algorithm is recomputed periodically, the planned trajectory being updated, as well as the associated control solutions.

For Navigation, a low-communication decentralised architecture is proposed. The full estimates of the relative state are computed at each s/c, avoiding a fully-connected communication network. In GTO, the access to GPS signals is not possible or very limited, and thus absolute positioning sensors are not available onboard. The navigation algorithm obtains its relative distance measurements from a RF system installed onboard. In order to update the estimates that are not locally estimated through the RF measurements, the state estimates communicated by another s/c are used as measurements. A correlation problem arises when the local states estimates are combined with the communicated state estimates, leading the Extended Kalman filter (EKF) to diverge. This problem can be avoided by using the Covariance Intersection (CI) algorithm [11]. However, the use of CI algorithm leads to reduced accuracy, since the error of the combined estimates is lower bounded by the error of the EKF. The filtering part of the estimation filter is divided in two steps: the calculation of the local state estimates through the local sensor measurements performed by the EKF, and the update of the remaining state vector variables, by using state estimates communicated by other s/c and combining them with the local estimates using the CI algorithm. Thus, a full-order filter, in the sense that the states estimates of all the formation s/c are computed at each s/c, is proposed.

The paper is organized as follows: in Section 2 we describe in detail the mission analysis and design for a 3 formation flying s/c in GTO. The GC algorithm is detailed in Section 3, while Section 4 focuses on the Navigation algorithm. Results of realistic simulations are presented for the GNC algorithms in Section 5. Section 6 provides conclusions and topics for work extensions.

2 ANALYSIS AND DESIGN OF FORMATION FLYING IN GTO

2.1 Design of a Demonstration Mission in GTO

A demonstration mission must recall both “Science requirements” and “Technology demonstration requirements”. The resulting mission timeline should be a consequence of merging the two set of requirements, in such a way that Formation Flying experiments are located in a specific and

convenient portion of the GTO orbit to enable interferometer observation. As one of the design drivers, the mission timeline shall be compatible with an exhaustive experiment implementation.

The set of requirements taken as inputs to the Mission Design task are hereafter outlined:

- **Science requirements** based on ESA's science cornerstone DARWIN, devoted to:
  - Detection and analysis of Earth-like planets orbiting nearby stars and
  - High resolution imaging by aperture synthesis.

- **Technology demonstration requirements**.
  - Flying precise formation manoeuvres.
  - Inter-satellite radio frequency ranging.
  - Inter-spacecraft high precision range (rate) laser metrology.
  - Micro-Newton thrusters (FEEP or cold gas).
  - Associated control software.

Considering these inputs, and after several iterations with ESA, a set of mission GNC modes was defined in the frame of the FEMDS study. These modes and their interrelationship are graphically depicted in Figure 1. Please note that the BCM mode only contemplates in this study the coarse acquisition of the spacecraft in order to be able to align and lock more accurate relative sensors (optical metrology) required to perform the scientific experiments. Fine relative control sub-modes within the BCM have not been considered as part of the study. The required conditions for mode transitions are defined in Table 1.

Figure 1: Mode sequence definition for FEMDS demonstration mission (left). Reference orbit for demonstration mission at GTO (right) with modes superimposed.

Table 1: Modes transition conditions

From	To	Formation configuration	Rel. position & vel. error transition conditions	Abs. attitude & attitude rate error transition conditions	Time/event condition	GNC equipment
From FAC	To ICM (To LFM)	Distance between s/c < 500 m. s/c plane orient. error < 5º	N/A	N/A	Fixed time to apogee	RF + star tracker (N) mN thrusters (C)
From LFM	To ICM	N/A	N/A	N/A	Fixed time to apogee	RF + star tracker (N) mN thrusters (C)
From ICM	To BCM	Distance between s/c 250m. Formation plane as observing plane	0.1 m, 1 cm/s	1 deg , 0.1 deg/s	Fixed time to apogee	RF + star tracker + divergent laser (N); mN thrusters (C)
From BCM	To LFM	N/A	N/A	N/A	Time of experiment	RF + star tracker; mN thrusters (C)

It is important to remark that the location in the orbit of the FAC mode is not fixed in advance and depends on many operational issues out of the scope of the study. Depending on its location FAC can be followed either by the ICM (situation called “FAC placed close-to-perigee”) or the LFM (“FAC centred on the apogee”). In this study, the second case was found to be more appropriate.

2.2 Formation Design Objectives and Drivers

The formation flying operation can be broadly grouped in two types of experiment: *tight formation* around apogee (during the experiment intervals) and *loose formation* out of apogee.

For the **tight formation phase**, the shape and orientation of the triangle formed by the three s/c is dictated by the direction of the target to be observed and by the imaging mode definition. Hence, in order to maximise the observation time, it is necessary to:

- Maintain constant the distances between s/c;
- Maintain constant the angle at reference s/c;
- Maintain constant the orientation of the formation plane;
- Facilitate, at exit of the experiment arc, the **natural return** of s/c to a configuration similar to the one needed to start the experiment at next apogee passage.

For the **loose formation phase**, the main driver was to maintain s/c in the range of the RF sensors still guaranteeing a collision safe configuration during perigee passage.

2.3 Design Process

Since the relative evolutions of s/c, in terms of positions and velocities, cannot be considered as design variables, it is preferable to rely the formation design on a constant (under Keplerian motion assumption) set of parameters, such as the relative Keplerian elements between the s/c composing the formation. The "Keplerian motion" assumption is valid in the case under consideration, since it is used for short periods of time (experiment durations around 2 or 4 hours) at the farthest point of orbit from the Earth (apogee). It is possible to establish a direct relationship between the relative Cartesian position and velocity (in the formation objectives side) and the variations δa, δe, $\delta\Omega$, δi, $\delta\omega$ and δM around the s/c nominal Keplerian elements (in the formation design process side), which are constant under the assumption of Keplerian motion, adopted for the first stages of design. This relationship is as follows [1]:

$$
\begin{aligned}
x_{1j}(\nu) &= \frac{a\sin\nu(2+e\cos\nu)}{1+e\cos\nu}\delta e + \frac{a(1-e^2)}{1+e\cos\nu}\cos i\,\delta\Omega + \frac{a(1-e^2)}{1+e\cos\nu}\delta\omega + \frac{a(1+e\cos\nu)}{\sqrt{1-e^2}}\delta M \\
y_{1j}(\nu) &= -\frac{a(1-e^2)}{1+e\cos\nu}\sin(\omega+\nu)\delta i + \frac{a(1-e^2)}{1+e\cos\nu}\sin i\cos(\omega+\nu)\delta\Omega \\
z_{1j}(\nu) &= -\frac{1-e^2}{1+e\cos\nu}\delta a + a\cos\nu\,\delta e - \frac{ae\sin\nu}{\sqrt{1-e^2}}\delta M
\end{aligned}
\qquad (1)
$$

Figure 2: Reference frame of the relative motion used for Formation Design purposes

where the Keplerian elements are: the true anomaly ν, the semi-major axis a, the eccentricity of the orbit e, the right ascension of the ascending node Ω, the inclination of the orbit i, the argument of perigee ω and the mean anomaly M. The relative position coordinates x_{1j}, y_{1j}, z_{1j}, j=2,3 (assuming that the hub is s/c 1 and that it is used as the reference) are referred to a frame as the one shown in Figure

2, centred at the hub, and with $\mathbf{k}_z$ axis pointing to nadir, $\mathbf{k}_y$ axis pointing in the same direction and opposite sense that the reference orbital angular motion vector ϖ_0, and $\mathbf{k}_x$ axis forming a right-handed system. This frame is designated as the Local Vertical Local Horizon (LVLH) frame.

Another frame of interest is the Inertial Planet Frame (IPQ), with the origin in the Earth mass centre, with $\mathbf{x}_{IPQ}$ axis parallel to the Earth vernal equinox direction, $\mathbf{z}_{IPQ}$ axis oriented towards North, and $\mathbf{y}_{IPQ}$ axis completing the frame.

Assuming a formation composed by three s/c, i.e., a hub and two telescope flyers, and that reference is set on the hub, the collection of conditions to impose are:

- Distance and distance evolution conditions.
- Angles between s/c and angles between s/c evolution conditions.
- Plane orientation and evolution conditions.

2.4 Design Results

Considering an inertial direction from central body to the apogee direction, and assuming a null difference in s/c mean semi major axes (δa_2,=0, δa_3,=0), the above conditions derive into a system of 10 non linear equations in [δe_2, δi_2, $\delta\Omega_2$, $\delta\omega_2$, δM_2] ; [δe_3, δi_3, $\delta\Omega_3$, $\delta\omega_3$, δM_3] that can be solved, after linearisation and particularisation at apogee, in the following way:

$$\begin{aligned}
&\delta a_2 = 0,\ \ \delta e_2 = 0,\ \ \delta i_2 = \frac{D}{a}\frac{\cos(\lambda-\alpha)}{1+e},\ \ \delta\Omega_2 = 0,\ \ \delta\omega_2 = \frac{D}{a}\frac{\sin(\lambda-\alpha)}{e(1+e)},\ \ \delta M_2 = -\frac{D}{a}\sqrt{1-e^2}\,\frac{\sin(\lambda-\alpha)}{e} \\
&\delta a_3 = 0,\ \ \delta e_3 = 0,\ \ \delta i_3 = \frac{D}{a}\frac{\cos\lambda}{1+e},\ \ \delta\Omega_3 = 0,\ \ \delta\omega_3 = \frac{D}{a}\frac{\sin\lambda}{e(1+e)},\ \ \delta M_3 = -\frac{D}{a}\sqrt{1-e^2}\,\frac{\sin\lambda}{e}
\end{aligned} \tag{2}$$

where D is the distance between satellites and α the angle at the reference s/c. λ is a design parameter. For the scope of this paper, selection of parameters is α=120º and λ=60º, with a commanded distance D=250m between the hub and the telescope flyers. The reference orbit shall have:

$$a = 26624.1\text{km},\ \ e = 0.73039,\ \ \Omega = 0,\ \ i = 7^\circ \ \text{ and } \ \omega = -\frac{\pi}{2}.$$

It is important to highlight that due to particularisation of equations around apogee, imposed conditions are not obtained for every anomaly value: the closer the anomaly to $\nu=\pi$, the better fulfilled are the imposed conditions. Moreover, imposed conditions on distance, angles and plane orientations are not achieved at all far from apogee. This is shown in Figure 3, where evolution of distance between s/c, angle at the hub (reference angle) and plane orientation is shown for different values of the mean anomaly. What these plots demonstrate is that, as required, the obtained design represents a stable option around apogee.

Figure 3: Open-loop evolution of distances (upper left), reference angle (upper right) and plane orientation (lower) propagating the spacecraft from an initial configuration provided by the design solution.

2.5 Optimisation of a Low-Thrust Control Law

An optimisation problem was stated as follows: find the optimal low thrust guidance laws for a set of three s/c flying in formation, such that for a time period of 4 hours centred on the apogee, the distance from the two telescope flyers to the hub keeps constant and equal to 250m; the angle at the hub keeps constant and equal to 120º; and the plane formed by the three s/c keeps constantly oriented towards apogee inertial direction.

In order to avoid s/c divergences during their travel out of apogee region, equality of semi major axes at the exit of the experiment phase was imposed as one additional condition. Results for the optimisation problem are shown in Figure 4a, in terms of figures of merit. Low thrust laws for these results resulted to be in the 0.1 to 1 mN level, for a S/C sized around 250 kg. Regarding the no-degradation condition out of the apogee region, Figure 4b also demonstrates the natural return, at apogee and after having run the experiment in the precedent orbit, to a relative state close to that corresponding to the start of a new experiment execution.

Figure 4a: Evolution of distances, reference angle and plane orientation of the spacecraft around apogee during a four hours experiment using optimal guidance profiles (to be used as feedforward commands) that tend to keep the observation parameters while simultaneously reaching a suitable configuration at the end.

Figure 4b: Evolution of distances, reference angle and plane orientation around the perigee starting from the end of a four hours experiment around apogee up to the start of next experiment.

3 GUIDANCE AND CONTROL

3.1 Relative formation Dynamics for Eccentric Orbits

The differential dynamics equations will be expressed with respect to the true anomaly ν, rather than to t. For elliptic orbits, the relation between t and ν is:

$$t - t_p = \frac{1}{n}\left[2\arctan\left(\sqrt{\frac{1-e}{1+e}} \tan\frac{\nu}{2} \right) - \frac{e\sqrt{1-e^2}\sin\nu}{1+e\cos\nu} \right] \tag{3}$$

where t_p is the passage time at perigee, and n is the natural frequency of the orbit.

Using the leader-follower technique [5], i.e., LVLH origin coincides with hub's mass centre (see Figure 2), we are interested in the relative motion of telescope flyers TF_2 and TF_3 with respect to the hub. As specified in Figure 5, $\boldsymbol{\rho}_i = \boldsymbol{\rho}_{1i} = \begin{bmatrix} x_{1i} & y_{1i} & z_{1i} \end{bmatrix}^T$ is the relative position vector between the hub (assumed as s/c 1) and TF_2 (i=2) or TF_3 (i=3), where $x_{1i} = x_i - x_1 = x_i$, $y_{1i} = y_i - y_1 = y_i$ and $z_{1i} = z_i - z_1 = z_i$, since $x_1 = y_1 = z_1 = 0$. The relative positions x_{1i}, y_{1i} and z_{1i} and the relative velocities $x'_{1i} = \frac{dx_{1i}}{d\nu}$, $y'_{1i} = \frac{dy_{1i}}{d\nu}$ and $z'_{1i} = \frac{dz_{1i}}{d\nu}$ characterize the state of TF_2 or TF_3 with respect to the hub.

Figure 5: Representation of the relative states between hub, TF_2 and TF_3

In LVLH, the set of linearised ν-varying equations describing the relative motion of telescope flyers TF_2 and TF_3 with respect to the hub is ([4], [5]):

$$\frac{d}{d\nu}\begin{bmatrix} x_{1i} \\ y_{1i} \\ z_{1i} \\ x'_{1i} \\ y'_{1i} \\ z'_{1i} \end{bmatrix} = \mathbf{A}_{s/c}(\nu)\begin{bmatrix} x_{1i} \\ y_{1i} \\ z_{1i} \\ x'_{1i} \\ y'_{1i} \\ z'_{1i} \end{bmatrix} + \frac{(1-e^2)^3}{(1+e\cos\nu)^4 n^2}\begin{bmatrix} 0 & 0 & 0 \\ 0 & 0 & 0 \\ 0 & 0 & 0 \\ 1 & 0 & 0 \\ 0 & 1 & 0 \\ 0 & 0 & 1 \end{bmatrix}\begin{bmatrix} f_{x,i} - f_{x,1} \\ f_{y,i} - f_{y,1} \\ f_{z,i} - f_{z,1} \end{bmatrix}, \quad \text{for } i=2,3. \tag{4}$$

where $\mathbf{A}_{s/c}(\nu)$ is the following 6×6 matrix:

$$\mathbf{A}_{s/c}(\nu) = \begin{bmatrix} 0 & 0 & 0 & 1 & 0 & 0 \\ 0 & 0 & 0 & 0 & 1 & 0 \\ 0 & 0 & 0 & 0 & 0 & 1 \\ \frac{e\cos\nu}{1+e\cos\nu} & 0 & \frac{-2e\sin\nu}{1+e\cos\nu} & \frac{2e\sin\nu}{1+e\cos\nu} & 0 & 2 \\ 0 & \frac{-1}{1+e\cos\nu} & 0 & 0 & \frac{2e\sin\nu}{1+e\cos\nu} & 0 \\ \frac{2e\sin\nu}{1+e\cos\nu} & 0 & \frac{3+e\cos\nu}{1+e\cos\nu} & -2 & 0 & \frac{2e\sin\nu}{1+e\cos\nu} \end{bmatrix} \tag{5}$$

Each external forces vector $\mathbf{f}_i = \begin{bmatrix} f_{x,i} & f_{y,i} & f_{z,i} \end{bmatrix}^T$ (i=1,2,3) includes the control inputs $\mathbf{u}_i$ acting on s/c i and the differential perturbations experienced by s/c i: $\mathbf{f}_i = \mathbf{u}_i + \sum \mathbf{w}_i$. The differential perturbations are the relative perturbations experienced by TF_2 and TF_3 with respect to the perturbations affecting the hub. In this paper, we consider $\sum \mathbf{w}_i = 0$. Nevertheless, the GC algorithms were tested in the presence of simulated perturbations, as reported in Section 5. Assuming also $\mathbf{u}_1 = \mathbf{0}$ (hub no controlled), then: $\mathbf{f}_i - \mathbf{f}_1 = \mathbf{u}_i - \mathbf{u}_1 = \mathbf{u}_i$, for i=2,3.

3.2 Model-Based Optimal Trajectory Planning

During FAC, the trajectories of TF_2 and TF_3 must minimize the propellant consumption, avoiding collisions. The state vector used in this GC section is:

$$\begin{aligned}\mathbf{X} &= \left[(\boldsymbol{\rho}_{12})^T \quad (\boldsymbol{\rho}'_{12})^T \quad (\boldsymbol{\rho}_{13})^T \quad (\boldsymbol{\rho}'_{13})^T\right]^T \\ &= \left[x_{12} \quad y_{12} \quad z_{12} \quad x'_{12} \quad y'_{12} \quad z'_{12} \quad x_{13} \quad y_{13} \quad z_{13} \quad x'_{13} \quad y'_{13} \quad z'_{13}\right]^T\end{aligned}$$

All control inputs are gathered into vector **U**:

$$\mathbf{U} = \left[u_{2,x} \quad u_{2,y} \quad u_{2,z} \quad u_{3,x} \quad u_{3,y} \quad u_{3,z}\right]^T$$

By gathering together the relative dynamics equations (4) for TF_2 and TF_3, the state equations of the optimal trajectory planning problem are:

$$\frac{d\mathbf{X}}{d\nu} = \mathbf{A}(\nu)\mathbf{X} + \mathbf{B}(\nu)\mathbf{U} \tag{6}$$

where:

$$\mathbf{A}(\nu) = \begin{bmatrix} \mathbf{A}_{s/c}(\nu) & \mathbf{0}_{6\times 6} \\ \mathbf{0}_{6\times 6} & \mathbf{A}_{s/c}(\nu) \end{bmatrix}$$

with $\mathbf{A}_{s/c}(\nu)$ expressed by (5). From (4), $\mathbf{B}(\nu)$ follows immediately.

The optimal trajectory planning problem is studied between ν_1 and ν_2, with $\nu_1 = \nu(t_1)$ and $\nu_2 = \nu(t_2)$ as provided by (3). Both the initial and the final state are given:

$$\mathbf{X}(\nu_1) = \mathbf{a} \quad \text{and} \quad \mathbf{X}(\nu_2) = \mathbf{b} \tag{7}$$

Each control inputs component U_j must satisfy:

$$u_{\min} \le |U_j| \le u_{\max}, \text{ for } j = 1,\ldots,6 \tag{8}$$

The cost function to be minimized is [6]:

$$J = \int_{\nu_1}^{\nu_2} \sum_{j=1}^{6} U_j^2 \, d\nu \tag{9}$$

By minimizing *J*, the overall control inputs are minimized. Since the control inputs are proportional to the propellant consumption, the propellant consumption is minimized.

3.3 Application of Pontryagin's Maximum Principle

We search for the optimal trajectories $\mathbf{X}^{opt}(\nu)$ and the associated optimal control inputs $\mathbf{U}^{opt}(\nu)$, which: respect the state equations (6), meet the two-boundary conditions (7), satisfy the control inputs limitations (8), and minimize the cost function (9). This optimal trajectory planning problem is solved by using PMP [7], where a co-state vector $\mathbf{\Lambda}$ is introduced:

$$\mathbf{\Lambda} = \begin{bmatrix} \lambda_1 & \lambda_2 & \lambda_3 & \lambda_4 & \lambda_5 & \lambda_6 & \lambda_7 & \lambda_8 & \lambda_9 & \lambda_{10} & \lambda_{11} & \lambda_{12} \end{bmatrix}^T$$

and 12 co-state equations are generated:

$$\frac{d\mathbf{\Lambda}}{d\nu} = \mathbf{C}(k)\mathbf{\Lambda}(k), \tag{10}$$

The PMP states that the control inputs which satisfy, for all $\nu_1 \le \nu \le \nu_2$, the stationarity conditions [6]:

$$\left.\begin{aligned} U_1^{opt} = u_{2,x}^{opt} &= -\frac{1}{2}\frac{(1-e^2)^3}{(1+e\cos\nu)^4 n^2}\lambda_4, \quad U_2^{opt} = u_{2,y}^{opt} = -\frac{1}{2}\frac{(1-e^2)^3}{(1+e\cos\nu)^4 n^2}\lambda_5, \\ U_3^{opt} = u_{2,z}^{opt} &= -\frac{1}{2}\frac{(1-e^2)^3}{(1+e\cos\nu)^4 n^2}\lambda_6, \quad U_4^{opt} = u_{3,x}^{opt} = -\frac{1}{2}\frac{(1-e^2)^3}{(1+e\cos\nu)^4 n^2}\lambda_{10}, \\ U_5^{opt} = u_{3,y}^{opt} &= -\frac{1}{2}\frac{(1-e^2)^3}{(1+e\cos\nu)^4 n^2}\lambda_{11}, \quad U_6^{opt} = u_{3,z}^{opt} = -\frac{1}{2}\frac{(1-e^2)^3}{(1+e\cos\nu)^4 n^2}\lambda_{12} \end{aligned}\right\} \tag{11}$$

are the optimal control inputs, the corresponding trajectory being optimal as well. By taking into account the linear relation (11) between the optimal control inputs and the co-state variables, the state equations (6) at ν_k become:

$$\left.\frac{d\mathbf{X}}{d\nu}\right|_k = \frac{\mathbf{X}(k+1)-\mathbf{X}(k)}{\delta\nu} = \mathbf{A}(k)\mathbf{X}(k) + \mathbf{B}^{\Lambda}(k)\mathbf{\Lambda}(k)$$

where $\mathbf{B}^{\Lambda}(k) = -\frac{1}{2}\left[\frac{(1-e^2)^3}{(1+e\cos\nu_k)^4 n^2}\right]^2 \begin{bmatrix} \mathbf{0}_{3\times3} & \mathbf{0}_{3\times3} & \mathbf{0}_{6\times6} \\ \mathbf{0}_{3\times3} & \mathbf{I}_3 & \\ \mathbf{0}_{6\times6} & & \mathbf{0}_{3\times3} \quad \mathbf{0}_{3\times3} \\ & & \mathbf{0}_{3\times3} \quad \mathbf{I}_3 \end{bmatrix}$. Finally, the recurrent expression of the state vector is:

$$\mathbf{X}(k+1) = \overline{\mathbf{A}}(k)\mathbf{X}(k) + \overline{\mathbf{B}}(k)\mathbf{\Lambda}(k) \tag{12}$$

where $\overline{\mathbf{A}}(k) = \delta\nu \cdot \mathbf{A}(k) + \mathbf{I}_{12}$ and $\overline{\mathbf{B}}(k) = \delta\nu \cdot \mathbf{B}^{\Lambda}(k)$.

Similarly, the co-state equations (10) become:

$$\mathbf{\Lambda}(k+1) = \overline{\mathbf{C}}(k)\mathbf{\Lambda}(k) \tag{13}$$

where $\overline{\mathbf{C}}(k) = \delta\nu \cdot \mathbf{C}(k) + \mathbf{I}_{12}$.

3.4 Algebraic Closed-Loop GC Algorithm

The two-boundary equations system to be solved consists of the state equations (12) and the co-state equations (13). Both initial and final state vectors are known (7), but no boundary condition is available for the co-state variables. This two-boundary equations system is solved by using the purely algebraic algorithm derived below, denoted "closed-loop GC algorithm". To take the unmodeled perturbations into account, as well as the state estimation errors, the closed-loop GC algorithm is recomputed periodically, at regularly spaced time instants (e.g., every 150s), and the planned optimal trajectory is updated.

Based on the recurrent expressions (12) and (13), $\mathbf{X}(k+1)$ and $\mathbf{\Lambda}(k+1)$ can be expressed directly as function of $\mathbf{X}(0)$ and $\mathbf{\Lambda}(0)$:

$$\mathbf{X}(k+1) = \mathbf{P}(k)\mathbf{X}(0) + \mathbf{Q}(k)\mathbf{\Lambda}(0) \tag{14}$$

$$\mathbf{\Lambda}(k+1) = \mathbf{N}(k)\mathbf{\Lambda}(0) \tag{15}$$

where **P**(*k*), **Q**(*k*) and **N**(*k*) are given by the following recurrent sequence:

(1) $\mathbf{P}(0) = \overline{\mathbf{A}}(0)$, $\mathbf{Q}(0) = \overline{\mathbf{B}}(0)$, $\mathbf{N}(0) = \overline{\mathbf{C}}(0)$

(2) FOR k=1 TO n-1

$$\mathbf{P}(k) = \overline{\mathbf{A}}(k)\mathbf{P}(k-1)$$

$$\mathbf{Q}(k) = \overline{\mathbf{A}}(k)\mathbf{Q}(k-1) + \overline{\mathbf{B}}(k)\mathbf{N}(k-1)$$

$$\mathbf{N}(k) = \overline{\mathbf{C}}(k)\mathbf{N}(k-1)$$

This recurrent sequence is nothing else than propagating dynamics between $\nu_1 = \nu_{k=0}$ and $\nu_2 = \nu_{k=n}$. The number of steps *n* is related to $\delta\nu$ by: $\delta\nu = \frac{\nu_2 - \nu_1}{n}$. We have: $\mathbf{X}(0) = \hat{\mathbf{X}}(\nu_1)$ and $\mathbf{X}(n) = \hat{\mathbf{X}}(\nu_2)$, so expression (14) written for *k*=*n*-1 becomes:

$$\mathbf{Q}(n-1)\mathbf{\Lambda}(0) = \mathbf{X}(\nu_2) - \mathbf{P}(n-1)\hat{\mathbf{X}}(\nu_1) \tag{16}$$

where $\mathbf{Q}(n-1)$ and $\mathbf{P}(n-1)$ are provided by the recurrent sequence. (16) is an algebraic system of 12 linear equations in $\mathbf{\Lambda}(0)$, i.e., the initial co-state variables at ν_1. This linear system is easily solved. Then, by means of (15), knowing $\mathbf{\Lambda}(0)$ we know all $\mathbf{\Lambda}(\nu)$, for $\nu_1 \le \nu \le \nu_2$. Finally, using the stationarity conditions (11), all optimal control inputs $\mathbf{U}^{opt}(\nu)$ are found. The optimal trajectories $\mathbf{X}^{opt}(\nu)$ are determined from (14).

The control inputs limitations (8) are considered only a posteriori. The obtained $\mathbf{U}^{opt}(\nu)$ are just not allowed to exceed the limitations: if component $\mathbf{U}_j^{opt}(\nu) > u_{\max}$, then $\mathbf{U}_j^{opt}(\nu) = u_{\max}$ is imposed. Collision avoidance is also ensured a posteriori: if the relative distance between two s/c becomes less than a safety distance, e.g., $D_{\min} = 40\text{m}$, then repulsive potential forces are applied to move them in opposite directions.

4 NAVIGATION

In the previous section, the GC algorithm was described, assuming noise-free full state availability. This section presents the algorithm used to estimate the formation flying s/c full state. A decentralized scheme is used, under which the state is fully estimated by each s/c of the fleet, based on measurements from the RF subsystem, and state estimates communicated by some neighbour s/c.

4.1 Formation Flying State Vector

Relative states are more convenient to represent the formation state than absolute states because measurements refer to relative distances between s/c and, should we consider the absolute state, the number of equations and variables to be determined by each s/c would lead to an undetermined

system, since there would be 6 variables, $x_j, y_j, z_j, x'_j, y'_j, z'_j$, to be determined and 3 measurements only per s/c (see subsection 4.3).

Therefore, the following extended version of the formation relative state vector for three s/c (see Figure 5) will be considered in this section:

$$\mathbf{X} = \left[(\boldsymbol{\rho}_{12})^T \quad (\boldsymbol{\rho}'_{12})^T \quad (\boldsymbol{\rho}_{13})^T \quad (\boldsymbol{\rho}'_{13})^T \quad (\boldsymbol{\rho}_{32})^T \quad (\boldsymbol{\rho}'_{32})^T \right]^T$$

where $\boldsymbol{\rho}_{32}$ and $\boldsymbol{\rho}'_{32}$ are only used in the navigation subsystem, but not passed to the GC algorithm, and

- ´ denotes the derivative with respect to the true anomaly ν, $\boldsymbol{\rho}' = \dfrac{d\boldsymbol{\rho}}{d\nu}$
- $\boldsymbol{\rho}_{ij} = \left[x_j - x_i \quad y_j - y_i \quad z_j - z_i \right]^T$ is the relative vector between s/c *i* and s/c *j*, where *i,j*=1,2,3.

Also, as already illustrated in Figure 5: $\boldsymbol{\rho}_{ij} = \boldsymbol{\rho}_j - \boldsymbol{\rho}_i = -\boldsymbol{\rho}_{ji}$, with $\boldsymbol{\rho}_i = \left[x_i \quad y_i \quad z_i \right]^T$.

4.2 Full-Order Decentralized Filter

From the navigation standpoint, a formation flying s/c fleet endowed with relative distance sensors and RF communications can be considered to have two underlying networks: a *communication network*, where linked s/c communicate state estimates, and a *measurement network*, linking each s/c to all the s/c it measures the relative distances to. In general, a s/c measures distances and communicates to any of its fleetmates. Nevertheless, it is desirable to reduce the number of measurements and especially the number of links in the communication network. The concept proposed in this work is to have each s/c measuring locally the distance to another fleet s/c (as expressed in the fleet *measurements network*), and transmitting its updated state estimates to another s/c (as expressed in the fleet *communications network*). The two networks are depicted in Fig. 6. The measurement network concerns the RF measurements of the distance with respect to another s/c, made every 20 seconds. The communication network concerns the communication between pairs of s/c, in order to send/receive the full state estimate between two spacecraft of the fleet. The state estimates are considered as observations in the receiving s/c.

The Navigation algorithm is based, at each s/c, on an EKF for local measurements, and on a CI algorithm (plus the EKF prediction part) for the measurements communicated by its linked s/c in the communications network. The CI algorithm [11] avoids the possible divergence of the EKF at the receiving s/c, due to correlation between measurements of the s/c in the fleet, especially when a token ring communication network topology is used (as it is the case for a 3-spacecraft fleet) by computing an upper bound for the covariance matrix of the fused variables. The price to pay is reduced estimation accuracy. Therefore, in the filtering step, the EKF is used when observations are measurements from the sensors, and the CI algorithm is applied whenever the observations are the state vector estimates from a s/c linked by the communications network.

Figure 6: a) Communication network b) measurement network

The full-order decentralized algorithm consists of two parts: prediction, similar to an EKF, and filtering, where the EKF filtering equations are replaced by the CI algorithm, when local measurements are replaced by state estimates communicated by another s/c.

Prediction

1. $\hat{\mathbf{X}}^i(k+1/k) = \mathbf{F}(k, \hat{\mathbf{X}}^i(k/k))$, where $\mathbf{F}(k, \hat{\mathbf{X}}^i(k \mid k))$ is approximated by a 4th-order four-stage Runge-Kutta method.
2. $\mathbf{P}^i(k+1/k) = \mathbf{\Phi}_k \mathbf{P}^i(k/k)(\mathbf{\Phi}_k)^T + \mathbf{Q}(k/k+1)$, where $\mathbf{Q}$ is the covariance matrix of the process noise, mainly due to unmodeled dynamics, and $\mathbf{\Phi}_k$ is the transition matrix $\mathbf{\Phi}_k \approx \mathbf{I} + \mathbf{F}(\hat{\mathbf{X}}^i(t), t)T_s + \frac{(\mathbf{F}(\hat{\mathbf{X}}^i(t), t)T_s)^2}{2!}$, where T_s is the sampling period used to propagate the estimate and i stands for the i^{th} s/c.

Filtering

For i=1,2,…, N-1, circularly (i.e., 1 comes after N-1)

Sensor Observation, $\mathbf{y}^i(k)$

1. Compute the local observation matrix: $\mathbf{H}^i(k, \hat{\mathbf{X}}^i(k \mid k-1))$ (the linearization of the original observation function – see subsection 4.3 - denoted by $\mathbf{H}^i(k)$ for simplification).
2. Compute the local innovation covariance matrix:

   $$\mathbf{S}^i(k) = \mathbf{H}^i(k)\mathbf{P}^i(k \mid k-1)(\mathbf{H}^i(k))^T + \mathbf{R}(k)$$

3. Compute the local Kalman Gain: $\mathbf{K}^i(k) = \mathbf{P}^i(k \mid k-1)\mathbf{H}^i(k)(\mathbf{S}^i(k))^{-1}$
4. Update local state estimate: $\hat{\mathbf{X}}^i(k/k) = \hat{\mathbf{X}}^i(k \mid k-1) + \delta\hat{\mathbf{X}}^i(k)$
5. Re-compute the local observation matrix: $\mathbf{H}^i(k, \hat{\mathbf{X}}^i(k \mid k))$
6. Compute the error covariance matrix:

   $$\mathbf{P}^i(k \mid k) = (\mathbf{I} - \mathbf{K}^i(k)\mathbf{H}^i(k))\mathbf{P}^i(k \mid k-1)(\mathbf{I} - \mathbf{K}^i(k)\mathbf{H}^i(k))^T + \mathbf{K}^i(k)\mathbf{R}^i(k)(\mathbf{K}^i(k))^T$$

State estimate from predecessor s/c, $\mathbf{z}^i(k) = \mathbf{X}(k \mid k-1) + \mathbf{v}^{i-1}(k)$

1. Compute the error covariance matrix:

   $$(\mathbf{P}^i(k \mid k))^{-1} = \omega(\mathbf{P}^i(k \mid k-1))^{-1} + (1-\omega)(\mathbf{P}^{i-1}(k \mid k-1))^{-1}$$

2. Update local state estimate:

   $$\hat{\mathbf{X}}^i(k \mid k) = \mathbf{P}^i(k \mid k)(\omega(\mathbf{P}^i(k \mid k-1))^{-1}\hat{\mathbf{X}}(k \mid k-1) + (1-\omega)(\mathbf{P}^{i-1}(k \mid k-1))^{-1}\mathbf{z}^i(k)),$$

   where the parameter ω is chosen at every step such that the trace of the matrix $\mathbf{P}^+_{k,i}$ is minimized.

4.3 RF Measurements

The relative distance measurements are based on pseudo-range RF signals, with the following mathematical model:

$$\rho_i^j = \left\|\boldsymbol{\rho}_i - \boldsymbol{\rho}_j\right\| + E^{i,j}_{multipath} + \varepsilon_\rho^{i,j} = \left\|\boldsymbol{\rho}_{ji}\right\| + \zeta_i \tag{17}$$

where:

- ρ_i^j is the code phase between transmitting spacecraft *i* and receiver spacecraft *j*, $\left\|\boldsymbol{\rho}_i - \boldsymbol{\rho}_j\right\| = \sqrt{(x_j - x_i)^2 + (y_j - y_i)^2 + (z_j - z_i)^2}$ is the equation that relates the true distance, between s/c *i* at time of signal transmission and s/c *j* at measurement time, with the formation state, in body reference frame (see Figure 7),
- $\varepsilon_\rho^{i,j}$ is the pseudo-range measurement noise due to the receiver thermal noise,
- $E_{multipath}^{i,j}$ represents the multi-path error.

When s/c *j* is receiving signals from s/c *i*, one must take into account the disposition of the three receiving antennas in the s/c, as depicted in Figure 7: for receiving antenna *k*: $\rho_i^{j,R_k} = \left\|\boldsymbol{\rho}_i - \boldsymbol{\rho}_j\right\|^{R_k} + E_{multipath}^{i,j} + \varepsilon_\rho^{i,j}$.

Figure 7: The three antennas, R_1, R_2, R_3, are placed in the sides of the s/c in the positions [*ap* 0 0], [0 *ap* 0], [0 0 *ap*] meters respectively with respect to the body frame. The measurement signals, $\rho_i^{j,R_1}, \rho_i^{j,R_2}, \rho_i^{j,R_3}$, transmitted from s/c *i*, are received by each antenna, R_1, R_2, R_3, on s/c *j*.

However the receiver antennas are not placed in the centre of the s/c, but placed *ap* meter ahead on each side of the s/c, as shown in Figure 7. Thus, there are three measurements instead of just one. Therefore, the relations between measurements received in the three antennas, $\rho_i^{j,R_1}, \rho_i^{j,R_2}, \rho_i^{j,R_3}$ and states expressed in the body reference frame are:

$$\begin{aligned} \left\|\boldsymbol{\rho}_i - \boldsymbol{\rho}_j\right\|^{R_1} &= \sqrt{(x_{ij}^b - ap)^2 + (y_{ij}^b)^2 + (z_{ij}^b)^2} \\ \left\|\boldsymbol{\rho}_i - \boldsymbol{\rho}_j\right\|^{R_2} &= \sqrt{(x_{ij}^b)^2 + (y_{ij}^b - ap)^2 + (z_{ij}^b)^2} \\ \left\|\boldsymbol{\rho}_i - \boldsymbol{\rho}_j\right\|^{R_3} &= \sqrt{(x_{ij}^b)^2 + (y_{ij}^b)^2 + (z_{ij}^b - ap)^2} \end{aligned} \tag{18}$$

Since the state vector is expressed in LVLH, the variables that are referred in the observations should be transformed into LVLH reference frame. Given the matrix $\mathbf{R}_b^{IPQ}$ transforming a position vector from the body frame to IPQ frame, the matrix transforming a relative position vector from LVLH to the s/c body frame is:

$$\mathbf{R}_{LVLH}^b = (\mathbf{R}_b^{IPQ})^T \mathbf{R}_{LVLH}^{IPQ}$$

Thus, any position vector **x** can be transformed from the body reference frame to LVLH frame by:

$$\mathbf{x}^{LVLH} = \mathbf{R}_b^{LVLH} \mathbf{x}^b$$

In particular:

$$\begin{bmatrix} x_{ij}^b & y_{ij}^b & z_{ij}^b \end{bmatrix}^T = \mathbf{R}_{LVLH}^b \begin{bmatrix} x_{ij}^{LVLH} & y_{ij}^{LVLH} & z_{ij}^{LVLH} \end{bmatrix}^T \text{ or } \begin{aligned} x_{ij}^b &= a_{11} x_{ij}^{LVLH} + a_{12} y_{ij}^{LVLH} + a_{13} z_{ij}^{LVLH} \\ y_{ij}^b &= a_{21} x_{ij}^{LVLH} + a_{22} y_{ij}^{LVLH} + a_{23} z_{ij}^{LVLH} \\ z_{ij}^b &= a_{31} x_{ij}^{LVLH} + a_{32} y_{ij}^{LVLH} + a_{33} z_{ij}^{LVLH} \end{aligned}$$

Applying the previous equation to the measurements given by equation (18), the observations obtained by receiving antenna 1 are then expressed in LVLH frame as follows:

$$\left\|\boldsymbol{\rho}_i - \boldsymbol{\rho}_j\right\|^{R_1} = \sqrt{\begin{aligned}&(a_{11}x_{ij}^{LVLH} + a_{12}y_{ij}^{LVLH} + a_{13}z_{ij}^{LVLH} - ap)^2 + (a_{21}x_{ij}^{LVLH} + a_{22}y_{ij}^{LVLH} + a_{23}z_{ij}^{LVLH})^2 \\ &+ (a_{31}x_{ij}^{LVLH} + a_{32}y_{ij}^{LVLH} + a_{33}z_{ij}^{LVLH})^2\end{aligned}}$$

and similarly for $\left\|\boldsymbol{\rho}_i - \boldsymbol{\rho}_j\right\|^{R_2}$ and $\left\|\boldsymbol{\rho}_i - \boldsymbol{\rho}_j\right\|^{R_3}$.

5 GNC RESULTS

The performance of the GNC algorithms was tested in the FF-FES realistic orbit dynamics simulator, developed by DEIMOS. With FF-FES it is possible to simulate open and closed-loop scenarios, calculating budget capabilities; Monte-Carlo processing and 2D&3D plots for analysis are also provided. Natural environment is simulated using a set of realistic and detailed models for the relative motion perturbations: solar radiation pressure, micro-meteoroids, atmospheric loads and higher order of Earth Gravity Field.

The results described in this section concern a GTO characterised by:

$$a = 26624.1\text{km},\ e = 0.73039,\ \Omega = 0,\ i = 7^\circ,\ \omega = -\frac{\pi}{2}.$$

The duration of FAC is chosen to be 6h, in order not to saturate the control inputs, which limitations are: $u_{\min} = 0.1\mu\text{N}$, $u_{\max} = 20\text{mN}$. The FAC centred on the apogee part of the orbit (see subsection 2.1) was chosen, because perturbations are less significant than close to perigee. More precisely, FAC starts at $t_1 = 10816.94\text{s}$ and ends at $t_2 = 32416.94\text{s}$, where the passage time at perigee $t_p = 0$. The corresponding true anomalies are (3): $\nu_1 = 156.5557^\circ$, $\nu_2 = 203.4442^\circ$.

The initial state $\mathbf{X}(\nu_1) = \mathbf{a}$ corresponds to a disposition of the three s/c within a sphere of 8km diameter, with velocities of maximum ±0.1m/s. In the estimation filter, this initial state has an error of 1m for the positions and 1m/rad for the velocities.

The final conditions $\mathbf{X}(\nu_2) = \mathbf{b}$ have been obtained using results from the optimal formation design task, in Section 2. Starting from these $\mathbf{X}(\nu_2) = \mathbf{b}$, after drift-free natural motion during next LFM, the goal is to attain, up to 1h before the next orbit's apogee, an isosceles triangle formation with 250m equal edges and a 120º angle between them. Table 2 presents $\mathbf{X}(\nu_1) = \mathbf{a}$ and $\mathbf{X}(\nu_2) = \mathbf{b}$, in IPQ.

Table 2. Initial and final states, in IPQ

	$\mathbf{X}(\nu_1) = \mathbf{a}$	$\mathbf{X}(\nu_2) = \mathbf{b}$
x_2[m]	-2400.0	203.56
y_2[m]	2018.5	-38.36
z_2[m]	-54.6	-20.40
$\dot{x}_2$[m/s]	-0.0473	-0.009191
$\dot{y}_2$[m/s]	-0.1038	-0.010179
$\dot{z}_2$[m/s]	0.0275	-0.002671
x_3[m]	-1273.8	-96.39
y_3[m]	-2557.0	-12.78
z_3[m]	-440.0	193.63
$\dot{x}_3$[m/s]	0.1401	0.005042
$\dot{y}_3$[m/s]	-0.0919	0.0045848
$\dot{z}_3$[m/s]	0.0089	-0.007274

The GNC closed-loop system integrates all the project work contributions. The formation flying s/c block is simulated by FF-FES, and provides sensor readings to the Navigation sub-system, which estimates the relative state and passes the relevant components to the GC subsystem. The latter uses mission specifications to provide the optimal torques to the formation flying s/c. In the closed-loop case, perturbations were disabled in the simulator, but the GNC algorithm had to handle sensor noise and mismatches between the dynamics model used by the GNC algorithms and the dynamics simulation.

Figures 8 and 9 show the GNC algorithms results. Figure 8 presents a projection in the *x*-*y* plane of the s/c optimal relative trajectories of TF2 and TF3, in IPQ. Figure 9 illustrates the performances of

the navigation algorithms, showing the evolution of the relative position error between the hub and TF_2. The plot shows that, though the estimator does not diverge, its relative stability is small. This is due to the difficulty in tuning the [18x18] covariance matrices of the measurement and the process noise and to the fact that, the covariance matrices not being diagonal, the change of a matrix term influences the estimation error for all the other state vector components. Furthermore, tuning the ω parameter of the CI algorithm has similar drawbacks, as improving the estimates for some state components will worsen others, if not done appropriately.

Figure 8: Projection in *x*-*y* plane of the optimal trajectories in IPQ of TF_2 (solid) and TF_3 (dashed)

Figure 9: Evolution of the relative position, between the hub and TF_2, estimation error

In terms of performance using closed-loop GNC, the error between the obtained final state $\mathbf{X}(\nu_2)$ and the desired one **b** is maximum 8m for position components and of 0.0012m/s for velocities. Simulations were also done without the estimator in the loop. In this case only GC is considered and, with all types of perturbations enabled in the simulator, the error is of the order of 0.1m for positions and of 0.0001m/s for velocities, which meets the mission conditions specified in Table 1 for the transition from FAC to BCM modes, with LFM and ICM included.

6 CONCLUSIONS

This paper introduced an integrated approach to GNC for a GTO formation flying spacecraft mission, encompassing novel mission design and analysis results, as well as guidance, navigation and control algorithms.

In this work, mission analysis has shown that it is possible for a typical GTO to obtain a highly stable 3 formation flying s/c for up to ~4 hours around apogee with low thrust laws in the order of 10^{-6}m/s². This enforces the feasibility of a possible scientific demonstration mission to be deployed at an Earth orbit, instead of targeting a more complex libration point orbit for these demonstration purposes.

Furthermore, it was demonstrated that, with appropriate formation design, it is possible to leave the spacecraft uncontrolled around perigee, between experiments, without risk of collision or need to spend excessive fuel to bring them together.

Concerning guidance and control, this paper presented a model-based optimal trajectory planning algorithm, our guidance-oriented approach consisting in regularly re-computing this algorithm. This (re)planning leads to trajectories that require less control effort during the trajectory tracking phase of the mission. The proposed optimal trajectory planning algorithm is based on the application of Pontryagin's Maximum Principle which, to the best of our knowledge, is novel for formation flying spacecraft GC.

As for the Navigation part, the formation state estimation is handled by a full-order decentralized estimator, based on the covariance intersection (CI) algorithm and an Extended Kalman Filter (EKF). The EKF is used for local measurements, while CI combines the local full state estimate with the estimate provided by a linked s/c in the *communications network*, eliminating EKF divergence. Our current work concerns the improvement of navigation performance, namely developing a multiple-weighted CI, by increasing the weights of relative distance and velocity estimates from predecessor s/c for state components not measured locally, as well as the weight of local estimates of state components measured locally. We are also studying individual s/c estimator stability, as well as the performance bounds of the problem [17], so as to evaluate how close to the optimal estimate is the suboptimal EKF and conclude on whether it is possible to meet the specified requirements when such an estimator is included in the loop. This is an important issue, often overviewed in the literature, which seldom considers the estimator in the loop. The solution for possible problems may be based on the usage of 2nd order terms in the EKF or of particle filters, which do not assume any particular probability distribution. Regarding formation stability [18], an analysis will be performed to ensure that the cooperation among the s/c is stable and robust to changes, despite the limitations in communications between s/c [19].

Simulation results with all GNC algorithms in closed loop have been presented, for a 3-spacecraft formation flying in a GTO, showing the ability to bring the three s/c from an initial location, inside a sphere of 8km in diameter, down to the specified triangle with distances in the order

of 200m between s/c. The GC results, without the estimator in the loop, meet the mission analysis specifications. The introduction of the estimator brings additional errors, which must be reduced in future work. Both absolute and relative attitude estimation and control will also be included in future work, based on sensor fusion between RF and star-tracker measurements. Additionally, the full implementation and test of the GNC algorithms for all the mission modes is envisaged.

REFERENCES

1. Schaub H., and Junkins, J. L.: *Analytical Mechanics of Space Systems*, AIAA Education Series, 2003.
2. Miele, A., Pritchard, R.E. and Damoulakis, J.N.: "Sequential Gradient Restoration Algorithm for Optimal Control Problems", *Journal of Optimization Theory and Applications*, vol. 5, nº4, 1970.
3. Robertson, A., Inalhan G., and J. How, "Formation control strategies for a separated spacecraft interferometer", in *American Control Conference*, vol. 6, June 1999, pp. 4142-4147.
4. Inalhan, G., Tillerson M.J., and How, J.P.: "Relative dynamics and control of spacecraft formations in eccentric orbits", *J. of Guidance, Control, and Dynamics*, vol. 25, No. 1, January-February 2002, pp. 48-59.
5. Tillerson, M.J.: *Coordination and Control of Multiple Spacecraft using Convex Optimization Techniques*, Master thesis, Massachusetts Institute of Technology (MIT), June 2002.
6. Dumitriu, D., Lima P., and Udrea, B.: "Optimal trajectory planning of formation flying spacecraft", in *Proceedings of the 16th IFAC World Congress*, July 4-8, 2005, Prague.
7. Bryson A.E., and Ho, Y.C.: *Applied optimal control*, Hemisphere Publishing Corporation, NY, 1975.
8. Smith R., and Hadaegh, F.: "Control topologies for deep space formation flying spacecraft", in *American Control Conference*, 2002.
9. Olfati-Saber, R., Dunbar, W.B., and Murray, R.: "Cooperative control of multi-vehicle system using cost graphs and optimisation", in *American Control Conference*, 2003.
10. Singh, G. and Hadaegh, F.: "Autonomous path-planning for formation flying applications", in *16th International Symposium on Space Flight Dynamics*, December 2002.
11. Arambel, P.O., Rago, C., and Mehra, R.K.: "Covariance Intersection algorithm for Distributed Spacecraft State Estimation", in *Proceedings of the America Control Conference*, Arlington, VA, 2001.
12. Fergunson, P.: *Distributed Estimation and Control Technologies for Formation Flying Spacecraft*, Master thesis, MIT, 2003.
13. Wertz, J.: *Spacecraft Attitude Determination and Control*, Astropysics and Space Science Library, vol. 73, Kluwer Academic Publishers, 1978.
14. Kang, B., Hadaegh F., and Scharf, D.: "Decentralized and self-centered estimation architecture for formation flying of spacecraft", in *16th International Symposium on Space Flight Dynamics*, Pasadena, California, December 2001.

15. Vallado, D. A.: *Fundamentals of Astrodynamics and Applications*, Space Technology Library, 2001
16. Sidi, M. J., Rycroft, M. J. (series editor), Shyy, W. (series editor): *Spacecraft Dynamics and Control: A Practical Engineering Approach*, Cambridge Aerospace Series, 1997
17. Van Trees, H. L. : *Detection, Estimation, and Modulation Theory: Part I*, Wiley, New York, 1968
18. Smith, R. S., and Hadaegh, F.: "Parallel Estimators and Communication in Spacecraft Formations", in *Proceedings of the IFAC World Congress*, Prague, July 2005
19. Fax J. A., and Murray, R. M.: "Information flow and cooperative control of vehicle formations", *IEEE Transactions Automatic Control*, 49(9):1465-1476, 2004

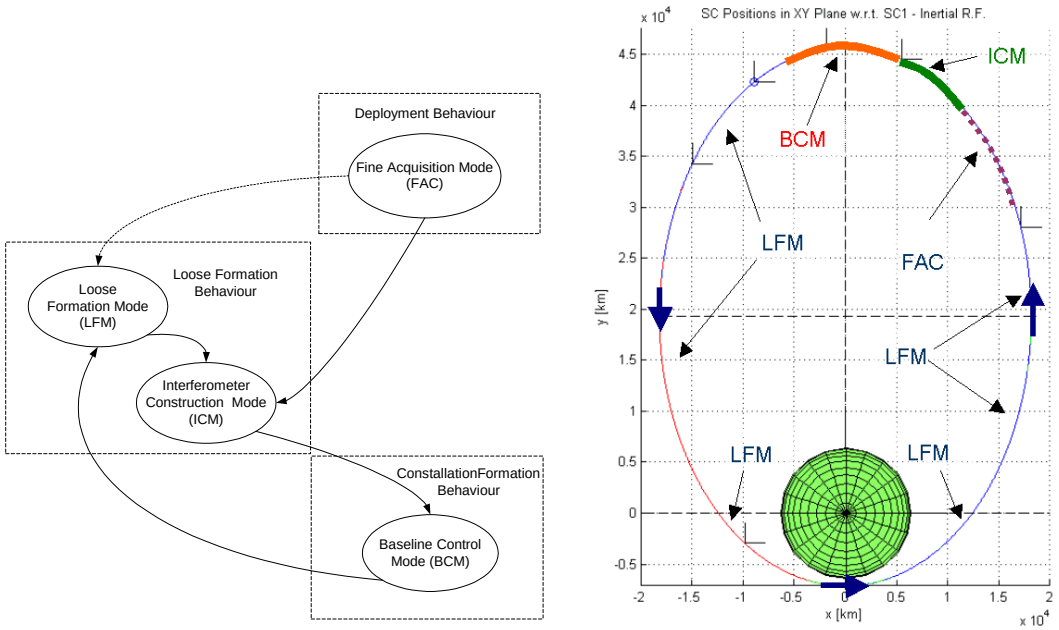

Figure 1: Mode sequence definition for FEMDS demonstration mission (left). Reference orbit for demonstration mission at GTO (right) with modes superimposed.

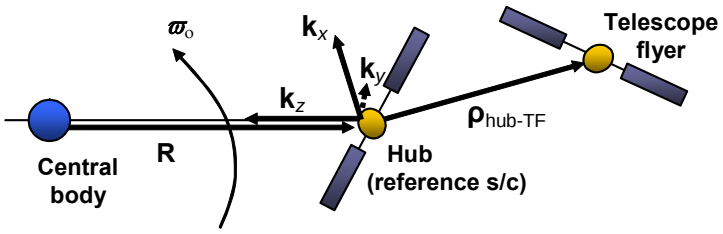

Figure 2: Reference frame of the relative motion used for Formation Design purposes

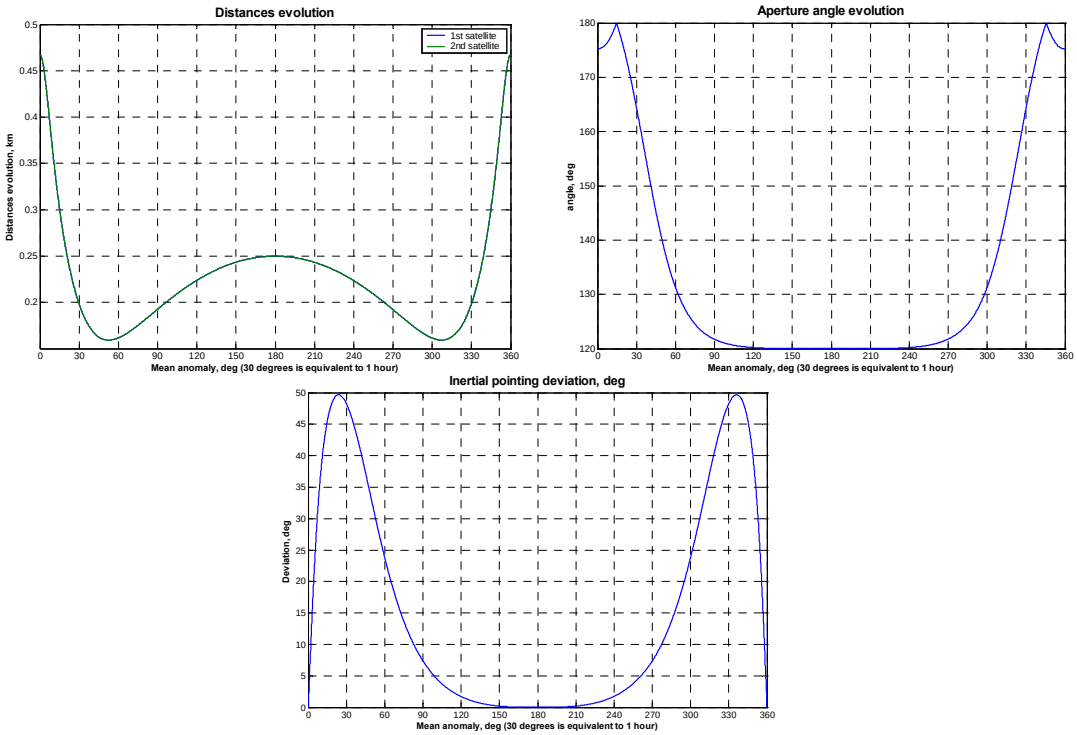

Figure 3: Open-loop evolution of distances (upper left), reference angle (upper right) and plane orientation (lower) propagating the spacecraft from an initial configuration provided by the design solution.

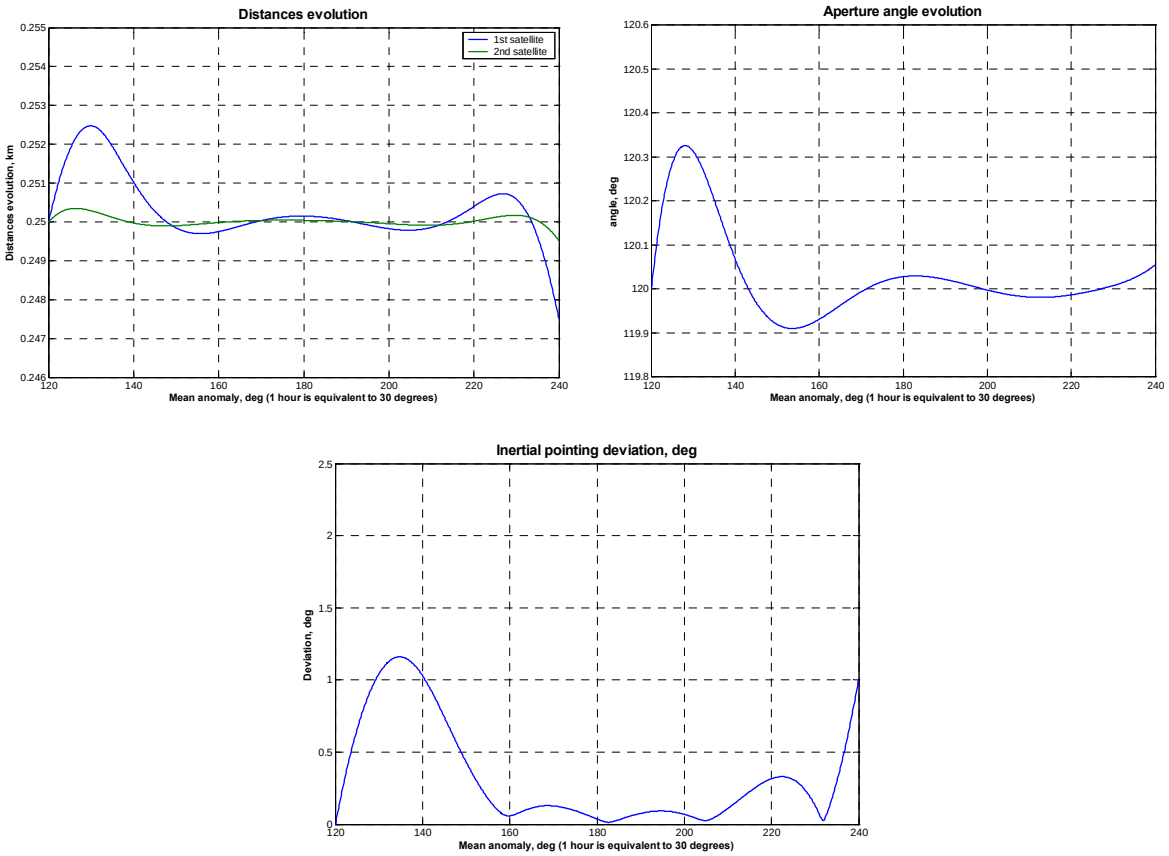

Figure 4a: Evolution of distances, reference angle and plane orientation of the spacecraft around apogee during a four hours experiment using optimal guidance profiles (to be used as feedforward commands) that tend to keep the observation parameters while simultaneously reaching a suitable configuration at the end.

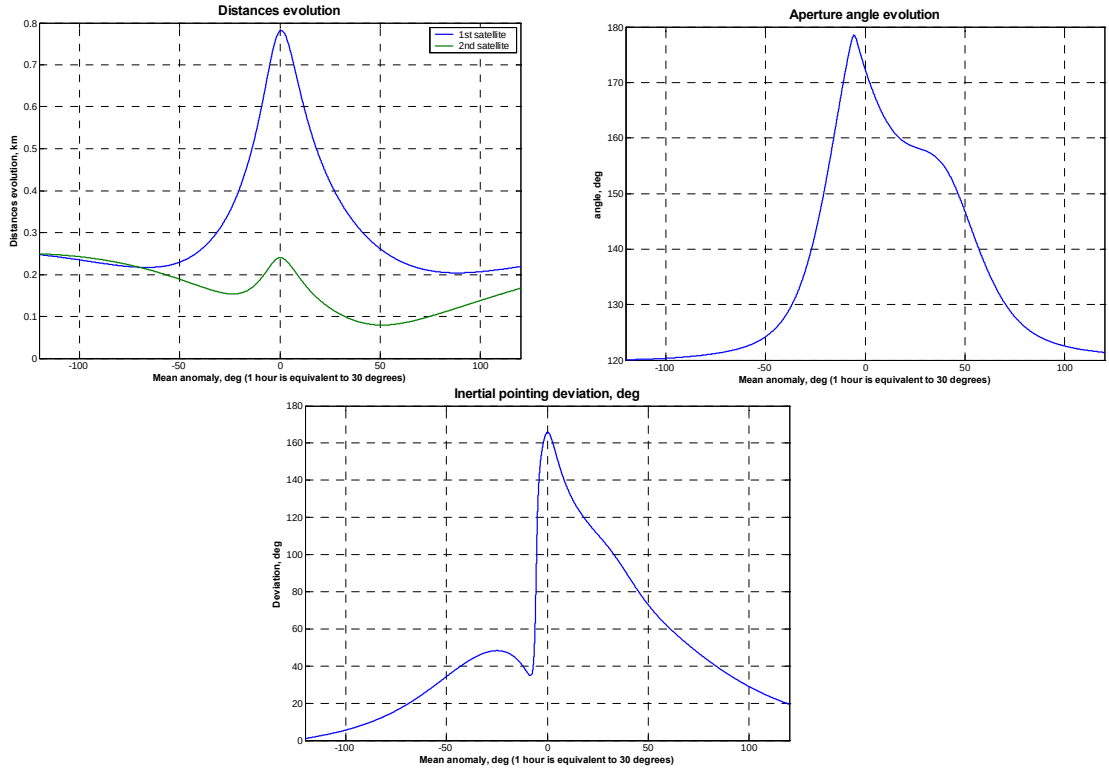

Figure 4b: Evolution of distances, reference angle and plane orientation around the perigee starting from the end of a four hours experiment around apogee up to the start of next experiment.

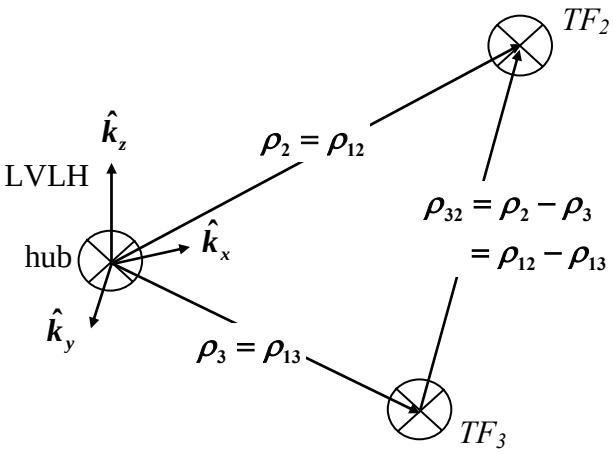

Figure 5: Representation of the relative states between hub, TF_2 and TF_3

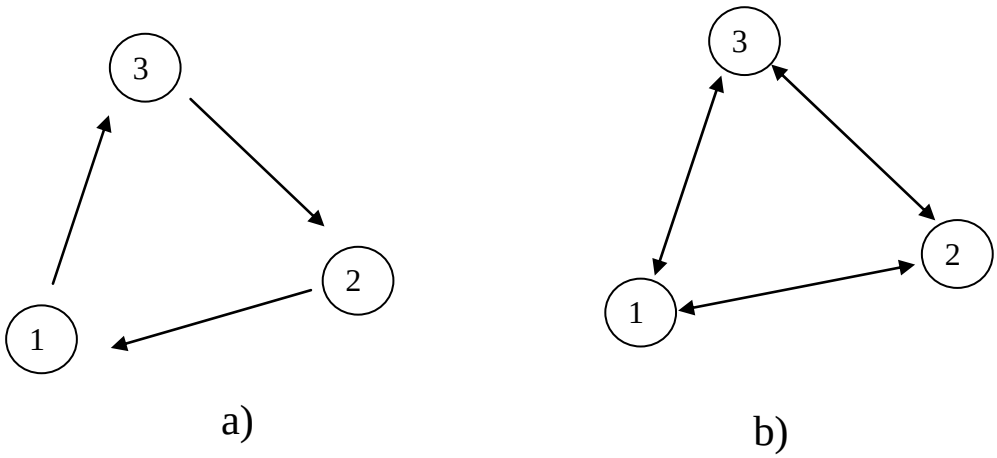

Figure 6: a) Communication network b) measurement network

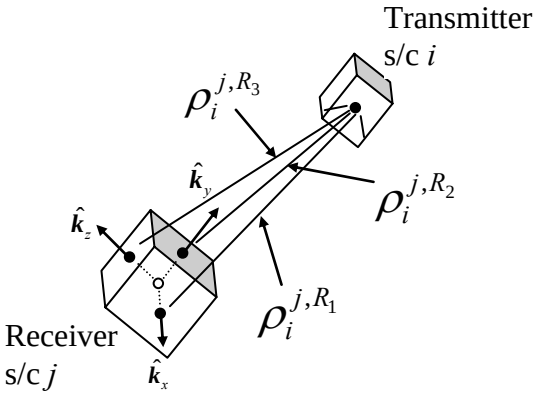

Figure 7: The three antennas, R_1, R_2, R_3, are placed in the sides of the s/c in the positions [*ap* 0 0], [0 *ap* 0], [0 0 *ap*] meters respectively with respect to the body frame. The measurement signals, ρ_i^{j,R_1}, ρ_i^{j,R_2}, ρ_i^{j,R_3}, transmitted from s/c *i*, are received by each antenna, R_1, R_2, R_3, on s/c *j*.

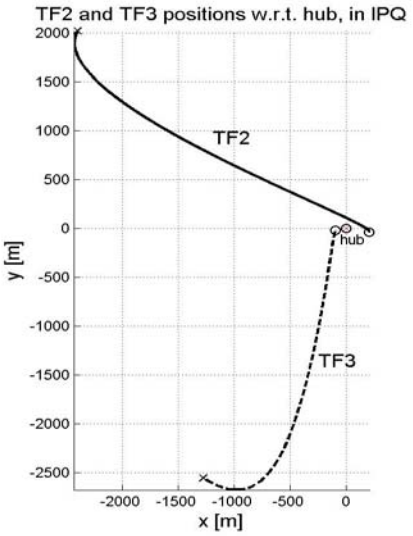

Figure 8: Projection in *x*-*y* plane of the optimal trajectories in IPQ of TF_2 (solid) and TF_3 (dashed)

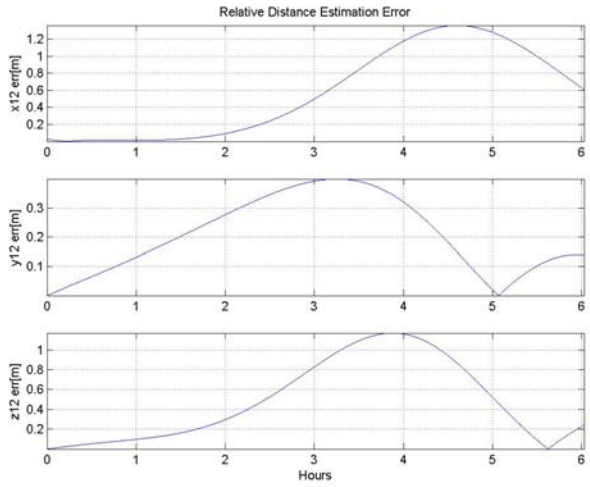

Figure 9: Evolution of the relative position, between the hub and $TF_{2,}$, estimation error